

# The nonlinear and distinct responses of ocean heat content and anthropogenic carbon to ice sheet freshwater discharge in a warming climate

Tessa Gorte<sup>1,2</sup>, Nicole S. Lovenduski<sup>1,2</sup>, Cara Nissen<sup>1,2</sup>, Jan T. M. Lenaerts<sup>1</sup>,  
Jeffrey B. Weiss<sup>1</sup>

<sup>1</sup>Department of Atmospheric and Oceanic Sciences, University of Colorado Boulder, Boulder CO, USA

<sup>2</sup>Institute of Arctic and Alpine Research, University of Colorado Boulder, Boulder CO, USA

## Key Points:

- We disentangle the linear and nonlinear effects of Greenland and Antarctic Ice Sheet melt on ocean heat content and anthropogenic carbon
- Future anthropogenic carbon storage and ocean heat content have disparate responses to separate and combined ice sheet melt in polar regions
- Greenland freshwater is more influential than Antarctic freshwater in driving future changes in anthropogenic carbon and ocean heat content

## Abstract

Anthropogenic climate change will drive extensive mass loss across both the Antarctic (AIS) and Greenland Ice Sheets (GrIS), with the potential for feedbacks on the global climate system, especially in polar regions. Historically, the high latitude North Atlantic and Southern Ocean have been the most critical regions for global anthropogenic heat and carbon uptake, but our understanding of how this uptake will be altered by future freshwater discharge is incomplete. Here, we assess each ice sheet's impact on the global ocean storage of anthropogenic heat and carbon for a high-emission scenario over the 21<sup>st</sup> century using a coupled Earth system model. Notably, combined AIS and GrIS freshwater engenders distinct anthropogenic heat and carbon storage anomalies as the two diagnostics respond disparately in the high latitude Southern Ocean and North Atlantic. We explore the impact of contemporaneous mass loss from both ice sheets on anthropogenic heat and carbon storage and quantify the linear and nonlinear contributions of each ice sheet. We find that GrIS mass loss exerts a primary control on the 21<sup>st</sup>-century evolution of both global oceanic heat and carbon storage, with AIS impacts appearing after the 2080s. Non-linear impacts of simultaneous ice sheets' discharge have a non-negligible contribution to the evolution of both heat and carbon storage. Further, anthropogenic heat changes are realized more quickly in response to ice sheet discharge than anthropogenic carbon. Our results highlight the need to incorporate both ice sheets actively in climate models in order to accurately project future global climate.

## Plain Language Summary

As the globe continues to warm in the next 100 years, the Antarctic and Greenland Ice sheets will continue to melt, adding freshwater to the surrounding ocean regions. This process is often poorly (if at all) represented in global climate models used to make projections about future climate change. Here, we simulate the climate response to melting ice sheets in a global climate model by adding freshwater to the model ocean near the edges of ice sheets. We focus our analysis on the impact of this freshwater addition on the future evolution of heat and carbon in the ocean, because both heat and carbon have the potential to feed back on the climate system (less heat/carbon in the ocean means more heat/carbon in the atmosphere and a warmer climate). By the end of the century, we find that the ocean stores less heat and carbon because of the melting ice sheets. We also find that summing the effects from melt on Antarctica and Greenland separately is not equal to the effect of melting both ice sheets simultaneously. Finally, we show that ocean heat and carbon respond differently to the same amount of ice sheet melt.

## 1 Introduction

The global ocean has taken up roughly a third of all anthropogenic emissions of CO<sub>2</sub> (C<sub>ANTH</sub>) over the course of the industrial period (Khatiwala et al., 2013; Gruber et al., 2023; Friedlingstein et al., 2022; DeVries et al., 2023) and over 90% of the excess heat over the last 50 years (Bindoff et al., 2007), thereby buffering the effects of climate change. The storage of excess heat and carbon is heavily dependent upon the physical and chemical state of the upper ocean including temperature, salinity, stratification, and carbonate chemistry (Maier-Reimer & Hasselmann, 1987; Sarmiento et al., 1992; Gruber et al., 2023). Cooler, more saline surface waters destabilize the water column, promoting surface-to-depth transport of C<sub>ANTH</sub> and excess heat and thereby facilitating more heat and carbon uptake at the surface (Terhaar et al., 2021). Over half of all anthropogenic carbon stored in the global ocean is found in the upper 400 m, with the Southern Ocean (SO) south of 35 °S alone accounting for over 40% of all C<sub>ANTH</sub> uptake (Gruber et al., 2019). Similarly, the SO south of 44 °S dominates the global ocean uptake of heat (89% of global ocean heat uptake; Huguenin et al., 2022). The North Atlantic is also a critical region for the uptake of excess heat and C<sub>ANTH</sub> fluxes as the Atlantic Meridional

Overturning Circulation (AMOC) drives surface-to-depth transport off the southern coast of the GrIS (Gruber et al., 2002; Huguenin et al., 2022), but recent/projected trends in global heat uptake were shown to be dominated by the SO (Huguenin et al., 2022).

With increased carbon emissions and subsequent anthropogenic warming, the global ocean  $C_{\text{ANTH}}$  inventory and the global excess ocean heat content ( $\text{OHC}_{\text{ANTH}}$ ) are projected to grow (Wanninkhof et al., 2013; Cheng et al., 2022; Terhaar et al., 2021; von Schuckmann et al., 2023), thereby shaping the trajectory of global climate change for the coming century and beyond (J. P. Abraham et al., 2013; Bronselaer et al., 2020; J. Abraham et al., 2022). Physical oceanographic changes will manifest first in the high latitudes (Manabe & Stouffer, 1980; Bintanja & Oerlemans, 1995; Holland & Bitz, 2003; Crook et al., 2011; Goosse et al., 2018) – including critical regions for heat and carbon uptake such as the Southern Ocean and the North Atlantic (Gruber et al., 2002; Khatiwala et al., 2013; Fletcher et al., 2006; Frölicher et al., 2015; Terhaar et al., 2021; Huguenin et al., 2022; Müller et al., 2023). Based on the 6<sup>th</sup> Coupled Model Intercomparison Project (CMIP6) ensemble average under Shared Socioeconomic Pathway 5-8.5 (SSP5-8.5), by the end of the 21<sup>st</sup> century, the upper ocean is projected to take up an additional 25 ZJ ( $1 \text{ ZJ} = 10^{21} \text{ J}$ ) of heat per year (Cheng et al., 2022) while anthropogenic carbon storage of the SO alone is projected to increase by  $\sim 200 \text{ Pg C}$  ( $1 \text{ Pg C} = 10^{15} \text{ g C}$ ) (Terhaar et al., 2021). At the same time, climate-driven strengthening of upper ocean stratification will weaken overturning and, consequentially, the ability of the ocean to transfer the excess heat and anthropogenic carbon to greater depths, thus reducing the global ocean's ability to buffer climate-change effects (Swingedouw et al., 2007; Davila et al., 2022; Gruber et al., 2023). Investigating their projected anthropogenic-driven changes, Bronselaer et al. (2020) find a linear relationship between global anthropogenic heat and carbon changes over the 21<sup>st</sup> century in the models assessed in their study, but none of these models accounted for the expected increasing future freshwater discharge from ice sheets.

One of the largest sources of projected oceanic change in the polar regions is melt-water from the Antarctic Ice Sheet (AIS) and the Greenland Ice Sheet (GrIS) which have been losing mass at rates of  $107 \text{ Gt y}^{-1}$  and  $261 \text{ Gt y}^{-1}$  ( $1 \text{ Gt} = 1 \text{ Gigaton} = 10^{12} \text{ kg}$ ), respectively, on average since 2002 (Velicogna et al., 2020). By 2100, the GrIS is expected to contribute  $90 \pm 50 \text{ cm}$  to global mean sea level under Representative Concentration Pathway 8.5 (RCP8.5; Goelzer et al., 2020). The trend of the AIS contribution to global mean sea level is less well constrained, and end-of-century estimates range from  $-7.6$  to  $30.0 \text{ cm}$  under the RCP8.5 scenario (Seroussi et al., 2020). Recent work demonstrated that ice sheet mass loss has significant ocean impacts, including surface cooling with subsurface warming, reduced deep convection and dense water formation, and, critically, strengthened upper ocean density gradients (Menviel et al., 2015; Pauling et al., 2016; Park & Latif, 2019; Bronselaer et al., 2020; Sadai et al., 2020; Nissen et al., 2022; Li, England, et al., 2023; Gorte et al., 2023). Yet, most CMIP6 models do not have an ice sheet component or the capability for ice sheets to interact with the other model components (Nowicki et al., 2016; N. Swart et al., 2023). In lieu of active ice sheet modeling in global climate models (GCMs), there have been many efforts to account for ice sheet freshwater (FW) through FW sensitivity experiments – testing different magnitudes, timing, duration, and location of FW input (Bintanja et al., 2013; N. C. Swart & Fyfe, 2013; Pauling et al., 2016; Bronselaer et al., 2018; Park & Latif, 2019; Sadai et al., 2020; Purich & England, 2023; N. Swart et al., 2023; Gorte et al., 2023). Acknowledging uncertainties arising from this one-way, ice sheet-to-ocean FW coupling approach, these studies have demonstrated robust changes to Southern Ocean physical properties (temperature, salinity, convection, etc.) when the ocean is subject to ice sheet FW input (Bintanja et al., 2013; N. C. Swart & Fyfe, 2013; Pauling et al., 2016; Bronselaer et al., 2018; Park & Latif, 2019; Sadai et al., 2020; Purich & England, 2023; Gorte et al., 2023).

As global ocean heat content and anthropogenic carbon uptake and storage are primarily controlled by physical oceanographic processes in the high latitudes, projected

ice sheet FW fluxes could have profound effects on these climatically important properties. Yet, their sensitivity to FW from individual and combined ice sheets remains understudied. Li, Marshall, et al. (2023) investigated the impact of AIS and GrIS FW discharge – individually and combined – on polar air, ice, and ocean properties. Leveraging linear convolution theory, they find that exceeding a melt rate threshold of  $\sim 5000$  Gt yr<sup>-1</sup> engenders a nonlinear climate response in surface air temperature, sea ice extent, AMOC, and Antarctic Bottom Water formation. Their study is one of the first to explore the (non)linearity in changes induced by ice sheet FW. As a result, we have little understanding of the potential nonlinearity of anthropogenic heat and carbon changes from ice sheet FW.

Here, we use the Community Earth System Model version 2 (Danabasoglu et al., 2020) to quantify and diagnose the role of ice sheet FW discharge in the 21<sup>st</sup>-century evolution of global OHC and anthropogenic carbon under the high-emission scenario Shared Socioeconomic Pathway 5-8.5 (SSP5-8.5). Our model sensitivity simulations are configured to separately assess the role of AIS and GrIS discharge, as well as the impact of their simultaneous melt. As we will demonstrate, OHC and anthropogenic carbon respond differently to ice sheet discharge, and nonlinearity is pervasive in our results. Further, machine learning-based analysis of our model output suggests that sea surface salinity (SSS) primarily drives changes in both quantities.

## 2 Methods

### 2.1 Model simulations with CESM2

We perform four coupled climate simulations with the Community Earth System Model version 2 (CESM2; Danabasoglu et al., 2020), which differ in the representation of FW fluxes from the AIS and GrIS and will be described in more detail below: (1) a control simulation, (2) an AIS simulation, (3) a GrIS simulation, and (4) a combined AIS and GrIS simulation – hereafter referred to as the AGrIS simulation. The control and AIS simulations are identical to those used in Gorte et al. (2023). Each simulation is run with a  $\sim 0.9 \times 1.25^\circ$  horizontal resolution under historical CMIP6 greenhouse gas forcing from 1970-2014 and under SSP5-8.5 greenhouse gas forcing from 2015-2100 (Meinshausen et al., 2020). The control simulation runs from 1970-2100 while the AIS, GrIS and AGrIS simulations branch off in 1992 and run until 2100.

In the control simulation, we do not allow for FW fluxes from either ice sheet to increase; instead, both ice sheets' FW contributions are held constant from 1970-2100. To achieve this, we override the default mechanism for mass preservation for the AIS in CESM2, i.e., the instantaneous transport of excess mass to the nearest coastal ocean grid cell as solid discharge when a 10 m of water equivalent mass threshold is exceeded. Instead, we point the model to prescribed solid and liquid flux values. The prescribed AIS FW discharge is the same for each month of the year: 1332 Gt in solid discharge and 1443 Gt in liquid discharge based on values reported by J. T. M. Lenaerts et al. (2015). Furthermore, we use findings reported in J. T. M. Lenaerts et al. (2015) to divide the AIS FW discharge across six ocean basins; each with its own ratio of solid-to-liquid fluxes (Figure 1). The FW flux values for the GrIS are derived from historical, active-Greenland CESM2 output which Noël et al. (2020) demonstrate yields realistic surface processes. In contrast to the AIS, the liquid FW discharge from the GrIS follows a strong seasonal cycle, peaking in July at 134 Gt and dropping to 0 Gt in the winter while the solid FW discharge is held constant over the annual cycle at 48 Gt. The GrIS FW discharge is also divided into six ocean basins based on Rignot et al. (2012). Annually, the combined solid and liquid discharge amounts to 2775 Gt y<sup>-1</sup> from the AIS and 1088 Gt y<sup>-1</sup> from the GrIS in total FW fluxes (Table S1). The fluxes are modeled as salinity fluxes and are applied to the coastal surface grid cells. The fluxes are area-weighted so that each grid cell contributes the same total FW flux.



In the AIS simulation, GrIS FW fluxes match those of the control simulation while the AIS produces increasing FW fluxes from 1992 to 2100. The AIS historical FW forcing is based on observational AIS mass balance data amalgamated by the Ice sheet Mass Balance Inter-comparison Exercise (IMBIE) team while the future FW forcing reflects recent results from ice sheet modeling (Rignot et al., 2019; DeConto et al., 2021). To produce the historical FW forcing, we apply a linear fit to the IMBIE team's AIS mass balance data such that the total AIS FW flux increases from 2775 Gt y<sup>-1</sup> in 1992 to ~3160 Gt y<sup>-1</sup> by 2020 (Figure 1; Rignot et al., 2019). To generate the future AIS FW flux forcing, we follow results published by DeConto and Pollard (2016). Using a combination of GCMs and ice sheet models under RCP8.5 atmospheric conditions, DeConto and Pollard (2016) project a roughly constant contribution from the AIS to the global mean sea level through ~2050 and a quasi-exponentially increasing contribution thereafter. Following these projections, our total AIS FW forcing increases linearly from 2775 Gt y<sup>-1</sup> to ~3160 Gt y<sup>-1</sup> from 1992 to 2020, remains at ~3160 Gt y<sup>-1</sup> from 2021 to 2050, and then increases nonlinearly from ~3160 Gt y<sup>-1</sup> to 9098 Gt y<sup>-1</sup> from 2051 to 2100 (Figure 1, Table S1). The IS-wide mass balance data from Rignot et al. (2019) indicate that much of the AIS mass loss is concentrated in the West Antarctic Ice Sheet (WAIS) region along the coasts of the Amundsen and Bellingshausen Seas (AB Seas; 95 °W to 145 °W). Therefore, we distribute the area-weighted, excess AIS FW evenly across the coastal ocean grid cells in the AB Seas ocean basin; preserving the solid-to-liquid FW discharge ratio. The FW fluxes from the five remaining AIS ocean basins all remain constant for the duration of the simulation.

In the GrIS simulation, AIS FW fluxes are held to the same constant value as in the control simulation while the GrIS FW fluxes increase. Although CESM2 has the capacity to actively model the GrIS (Noël et al., 2020), we take the same approach here for overriding the default FW fluxes as in the AIS simulation to generate comparable output. For the entire 1992-2100 simulation period, GrIS FW fluxes for each basin follow exponential curves fit to the CESM2 GrIS FW output (ensemble member 1) generated for CMIP6 (Danabasoglu et al., 2020). The GrIS-integrated, total FW discharge increases from 1088 Gt y<sup>-1</sup> in 1992 to 2868 Gt y<sup>-1</sup> in 2100 while the total solid-to-liquid ratio decreases from 52%-48% to 8%-92% (Figure 1). This drastic change in solid-to-liquid ratio accounts for the severely diminished solid ice fluxes as the GrIS ablation zone retreats further inland, reducing the ice-ocean interface (J. T. Lenaerts et al., 2019). As mass loss is more ubiquitous throughout the ablation zone along the GrIS periphery, the FW fluxes are applied around the entire GrIS coast and have disparate rates of solid and liquid discharge change across basins (Figures S2-S3). As with the AIS, the FW is applied to the coastal surface grid cells and area-weighted such that each grid cell is contributing equal amounts of total FW.

Lastly, in the AGrIS simulation, we override both ice sheets' default mass threshold, instead applying the increasing FW forcing, detailed above, for each IS simultaneously. The response of the AIS, GrIS, and AGrIS simulations, then, is directly comparable.

## 2.2 Quantifying Linear and Nonlinear Impacts from added Freshwater

We quantify the relative strength of the linear and nonlinear response of a given scalar global climate diagnostic  $d$  to the single- and combined-IS FW input using the four simulations. For our analyses, we use  $\text{OHC}_{\text{ANTH}}$  and  $\text{C}_{\text{ANTH}}$  as diagnostics. For the three perturbation experiments  $X = \text{AIS}, \text{GrIS}, \text{AGrIS}$ , we define the anomaly diagnostic  $d^X(t)$  as the difference between experiment  $X$  and the control at time  $t$ . We consider how the climate response depends on the cumulative FW discharge by time  $t$  integrated across an ice sheet,  $\text{FW}_X(t)$ , where  $X$  is either *AIS* or *GrIS*. We apply a 10-year moving mean to  $d^X(t)$  to smooth over fast internal climate variability.

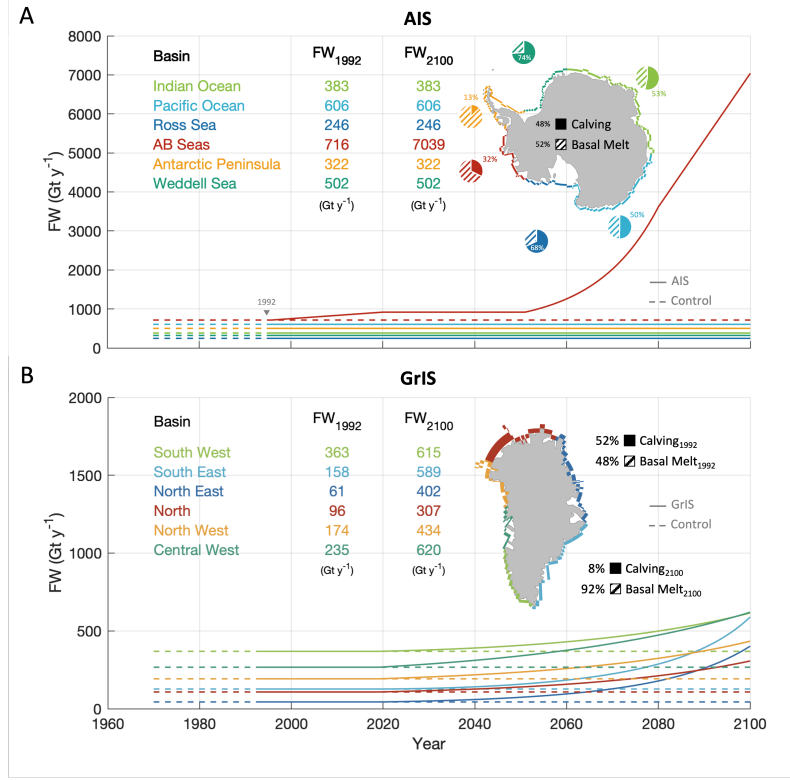


**Figure 1.** (A) Spatial distribution and temporal evolution of the total freshwater (FW) in  $\text{Gt y}^{-1}$  flux for each Antarctic Ice Sheet (AIS) basin: the Indian Ocean (light green), the Pacific Ocean (light blue), the Ross Sea (dark blue), the Amundsen and Bellingshausen (AB) Seas (red), the Antarctic Peninsula (orange), and the Weddell Sea (dark green). The pie charts depict the solid-to-liquid FW flux ratio as calving (filled) and basal melt (dashed) where the percentages denote calving based on J. T. M. Lenaerts et al. (2015). Also displayed are the calving and basal melt percentages for the integrated AIS (black). The values displayed are the initial (1992) and final (2100) basin-integrated FW fluxes in  $\text{Gt y}^{-1}$ . The time series show the temporal evolution of the basin-integrated FW fluxes for the period (1970-2100) for the control (dashed) and AIS (solid) simulations. (B) Same as panel (A) but for the Greenland Ice Sheet (GrIS) and GrIS basins: South West (light green), South East (light blue), North East (dark blue), North (red), North West (orange), and Central West (dark green). The solid-to-liquid FW flux ratios fluctuate with time for each GrIS basin with the 1992 percentages shown to the upper right of the GrIS map and 2100 to the lower right in black. For more information on the solid-to-liquid FW flux ratio, see Figures S2-S3. (1 Gt = 1 Gigaton =  $10^{12}$  kg.)

The first step in the decomposition is to perform linear fits of the AIS and GrIS experiments, resulting in linear coefficients  $\ell_{\text{AIS}}$  and  $\ell_{\text{GrIS}}$ . This defines the linear responses  $\text{AIS}_{\text{linear}} = \ell_{\text{AIS}} \text{FW}_{\text{AIS}}$ ,  $\text{GrIS}_{\text{linear}} = \ell_{\text{GrIS}} \text{FW}_{\text{GrIS}}$ . Then the total climate responses in the single-IS forcing experiments are

$$d^{\text{AIS}}(t) = \text{AIS}_{\text{linear}} + \text{AIS}_{\text{nonlinear}}, \quad (1)$$

$$d^{\text{GrIS}}(t) = \text{GrIS}_{\text{linear}} + \text{GrIS}_{\text{nonlinear}}. \quad (2)$$

The combined-IS forcing experiment AGrIS has an additional response,  $\text{IS}_{\text{combined}}$ , due to the nonlinear interaction of  $\text{FW}_{\text{AIS}}$  and  $\text{FW}_{\text{GrIS}}$

$$d^{\text{AGrIS}}(t) = d^{\text{AIS}}(t) + d^{\text{GrIS}}(t) + \text{IS}_{\text{combined}}. \quad (3)$$

The single-IS nonlinear responses are obtained from the subtracting the total responses in the single-IS forcing simulations from the linear response. Then the combined-IS nonlinear response is obtained from subtracting the total combined-IS response from the sum of the single-IS responses.

We calculate the linear fits for each 20-year segment starting in 2000, and average them to get the final  $\ell_{\text{AIS}}$ ,  $\ell_{\text{GrIS}}$  for each diagnostic. The  $\ell$  coefficients vary by  $\sim 10\%$  depending on the length of segments (5-, 10-, 20-, and 25-year; not shown). We track the temporal evolution of each term to measure the relative response to linear and nonlinear single-IS FW fluxes as well as to the nonlinear, combined-IS FW fluxes.

### 2.3 Using Gaussian Process Regression to disentangle contributors to $\text{OHC}_{\text{ANTH}}$ and $\text{C}_{\text{ANTH}}$ anomalies

Changes in  $\text{OHC}_{\text{ANTH}}$  and  $\text{C}_{\text{ANTH}}$  in response to added freshwater are caused by a complex interplay of changes in water-mass properties, sea ice and circulation. Here, we identify the different driving factors in the linear and nonlinear  $\text{OHC}_{\text{ANTH}}$  and  $\text{C}_{\text{ANTH}}$  responses testing a suite of 24 predictive models in MATLAB's Regression Learner toolbox. We supply five input variables as predictors: AMOC, sea surface salinity (SSS), sea surface temperature (SST), Arctic sea ice extent ( $\text{SIE}_{\text{NH}}$ ), and Antarctic sea ice extent ( $\text{SIE}_{\text{SH}}$ ). With each predictor impacting surface-to-depth transfer, water-column stratification or air-sea fluxes, these five predictors represent quantities critical for anthropogenic heat and carbon storage (Bronse laer et al., 2020).

Of all tested predictive models including Gaussian Process Regression (GPR) models, linear regressions, random forest decision trees, and neural networks, the exponential GPR model produced the lowest root-mean-square error (RMSE) between its predicted output and the two CESM-simulated diagnostics of interest, i.e.,  $\text{OHC}_{\text{ANTH}}$  and  $\text{C}_{\text{ANTH}}$ . GPR models do not directly yield information about the relative importance of each predictor. As such, we sequentially decompose our kernel function by withholding one predictor at a time and recording the subsequent RMSE. The resulting RMSE values for each withheld predictor, then, indicate their relative importance; withholding the most important predictor(s) generates the highest error between the predictive model and the CESM-simulated  $\text{OHC}_{\text{ANTH}}$  or  $\text{C}_{\text{ANTH}}$ .

## 3 Results

### 3.1 Model Validation

Globally-integrated  $\text{OHC}_{\text{ANTH}}$  simulated by CESM2 is well aligned with observation-based estimates, but regional biases persist particularly in the high latitude and subpolar North Atlantic, subpolar South Atlantic, and eastern tropical Pacific. Interpolated *insitu* observations from the World Ocean Database estimate the global, upper 2000 m  $\text{OHC}_{\text{ANTH}}$  in 2020 to be 234 ZJ and 211 ZJ, respectively (Cheng et al., 2021). Compared

to 1981, CESM2 produces a 255 ZJ global anomaly in 2020 in the upper 2000 m. The slight overestimation in CESM2 could at least partially be explained by the absence of the warming hole in and around the Irminger Sea in the high latitude North Atlantic and the broad warming patterns in the subpolar North and South Atlantic basins in the model (Figure S5). Similarly, CESM2 overestimates the negative  $\text{OHC}_{\text{ANTH}}$  response in the eastern tropical Pacific. Acknowledging these discrepancies, CESM2 produces global  $\text{OHC}_{\text{ANTH}}$  estimates in general good agreement with observation-based estimates (Cheng et al., 2021).

As for  $\text{OHC}_{\text{ANTH}}$ , historical CESM2  $\text{C}_{\text{ANTH}}$  is in generally good agreement with reconstructed observations. Sabine et al. (2004) estimate  $106 \pm 17$  Pg C for global 1994  $\text{C}_{\text{ANTH}}$ , integrated over the entire water column. For the same year, CESM estimates 85 Pg C of globally integrated anthropogenic carbon storage, 4 Pg C below the bottom of the range given by Sabine et al. (2004). Long et al. (2021) find that CESM2 reproduces  $\sim 75\%$  of the observed  $\text{C}_{\text{ANTH}}$ , arguing that the discrepancy is the result of poor thermocline ventilation and the omission of pre-1850  $\text{C}_{\text{ANTH}}$  in the model. The largest stores of historical  $\text{C}_{\text{ANTH}}$  occur in the North Atlantic where both observed and CESM2-simulated values range from  $\sim 60 - 80$  Pg C (compare Fig. 1 to Sabine et al., 2004).

### 3.2 $\text{OHC}_{\text{ANTH}}$ and $\text{C}_{\text{ANTH}}$ anomalies in response to ice sheet Freshwater Discharge

By the year 2100, the global ocean stores less anthropogenic ocean heat and carbon when both ice sheets melt, but the temporal evolution of the anomalies in response to freshwater from AIS or GrIS is distinct for the two diagnostics (Figure 2, Table S3). Freshwater discharge from the Antarctic Ice Sheet anomalously increases anthropogenic ocean heat content relative to the control simulation until the year 2095 while freshwater discharge from the Greenland Ice Sheet already anomalously decreases ocean heat content after  $\sim 2040$  (compare blue and red lines in Figure 2A). In the control simulation,  $\text{OHC}_{\text{ANTH}}$  increases from  $\sim 1450$  ZJ in 1992 to  $\sim 4500$  ZJ in 2100 (Figure S6A). From 1992 to 2010, anomalous  $\text{OHC}_{\text{ANTH}}$  responds similarly in the AIS and GrIS (Figure 2A). For this period, the AIS simulation stores an additional +19.7 ZJ of anomalous  $\text{OHC}_{\text{ANTH}}$  compared to +12.3 ZJ in the GrIS simulation (Table S3). The AIS anomaly grows to +25.1 ZJ during the 2030-2050 period and peaks in 2052 at 71.9 ZJ (blue line in Figure 2A) which corresponds to +5.1% of the 1992 globally-averaged control  $\text{OHC}_{\text{ANTH}}$ . Averaged over the same 2030-2050 period, the GrIS anomaly decreases to +4.7 ZJ (red line). By the end of the simulation period from 2080-2100, the AIS anomaly is lower than at its peak but is still anomalously higher than the control simulation (+2.9 ZJ; Table S3). Comparatively, anomalous  $\text{OHC}_{\text{ANTH}}$  in the GrIS simulation declines substantially through the latter half of the 21<sup>st</sup> century, resulting in a -26.3 ZJ reduction of anomalous global  $\text{OHC}_{\text{ANTH}}$  over 2080-2100 (Table S3).

In the simulation with simultaneous freshwater discharge from the Greenland and Antarctic ice sheets (AGrIS), the temporal evolution of  $\text{OHC}_{\text{ANTH}}$  anomalies tracks that of the Antarctic Ice Sheet in the early part of the century and of the Greenland Ice Sheet in the later part of the century (black line in Figure 2A). Averaged from 2030 to 2050, the global ocean stores 23.5 ZJ more heat in the AGrIS simulation than in the control simulation (1.6 ZJ less than the AIS simulation and 18.8 ZJ more than the GrIS simulation). As with the AIS and GrIS simulations, anomalous  $\text{OHC}_{\text{ANTH}}$  trends negatively after 2050 in the AGrIS simulation (Figure 2A). The negative trend in the AGrIS simulation drives a -42.6 ZJ loss in anomalous global  $\text{OHC}_{\text{ANTH}}$  over the last 20 years of the simulation (45.5 ZJ less than the AIS simulation and 17.3 ZJ less than the GrIS simulation).

Freshwater discharge from the Antarctic Ice Sheet rapidly reduces anthropogenic carbon storage in the global ocean until 2050, whereas freshwater discharge from the Greenland Ice Sheet produces rapid reductions in global anthropogenic carbon storage after

**Table 1.** Global  $\text{OHC}_{\text{ANTH}}$  and  $\text{C}_{\text{ANTH}}$  anomalies averaged over each time period from each of the simulations.

	$\text{OHC}_{\text{ANTH}}^{\dagger}$			$\text{C}_{\text{ANTH}}^{\ddagger}$		
	1992-2010	2030-2050	2080-2100	1992-2010	2030-2050	2080-2100
AIS	+19.7	+25.1	+2.9	+0.05	-0.56	-0.93
GrIS	+12.3	+4.7	-26.3	+0.19	-0.11	-1.90
AGrIS	+10.7	+23.5	-42.6	+0.07	-0.47	-2.09

$\dagger$  ZJ  
 $\ddagger$  Pg C

2040, dropping to anomalously negative values after 2070 (Figure 2B). For the 1992-2010 period, the AIS and GrIS simulations accumulate 0.05 Pg C and 0.19 Pg C more  $\text{C}_{\text{ANTH}}$ , globally, than the control simulation, respectively (Table 1), which is small compared to the overall increase from 87 Pg C in 1992 to 516 Pg C in 2100 in the control simulation (Figure S6B). By the middle of the simulation (2030-2050), both the AIS and GrIS simulations store anomalously less  $\text{C}_{\text{ANTH}}$ . During this period, the AIS simulation stores less  $\text{C}_{\text{ANTH}}$  than the GrIS simulation at -0.56 Pg C compared to -0.11 Pg C, respectively (Table 1). This dynamic flips by the end of the simulation as the GrIS simulation stores -1.90 Pg of anomalous global  $\text{C}_{\text{ANTH}}$ ; 0.97 Pg C less than the -0.93 Pg C stored in the AIS simulation (Table 1). The differences between the 2030-2050 and 2080-2100 periods are largely due to the changing AIS simulation response which, after peaking in magnitude in 2053 at -1.5 Pg C (-1.8% of the 1992 globally-averaged Control  $\text{C}_{\text{ANTH}}$ ), stabilizes at around  $\sim -1.0$  Pg C from 2050-2100 (Figure 2B).

While initially resembling the response from Antarctic Ice Sheet FW,  $\text{C}_{\text{ANTH}}$  in the AGrIS simulation is more analogous to that of the GrIS simulation by the end of the simulation (Figure 2B). For both the 1992-2010 and 2030-2050 periods, the AGrIS simulation response mirrors that of the AIS simulation more closely, engendering +0.07 Pg and -0.47 Pg  $\text{C}_{\text{ANTH}}$  anomalies, respectively (Table 1). Like the AIS simulation, the magnitude of the AGrIS  $\text{C}_{\text{ANTH}}$  anomaly decreases after peaking in the 2050s, but, unlike the AIS simulation, trends negatively after 2070, resulting in a final -2.09 Pg  $\text{C}_{\text{ANTH}}$  anomaly from 2080-2100 (Figure 2B). Ultimately, the AGrIS simulation stores 1.16 Pg less  $\text{C}_{\text{ANTH}}$  than the AIS simulation and 0.19 Pg less  $\text{C}_{\text{ANTH}}$  than the GrIS simulation from 2080 to 2100 (Table 1).

In addition to the distinct temporal evolution, spatial patterns differ for the uptake and storage of  $\text{C}_{\text{ANTH}}$  and  $\text{OHC}_{\text{ANTH}}$ . Historically,  $\text{C}_{\text{ANTH}}$  is largely stored in the North Atlantic while  $\text{OHC}_{\text{ANTH}}$  is prevalent throughout the Atlantic Ocean in both hemispheres as detailed in Section 3.1 (1970-1990; Figure 3A&B). The polar oceans store little  $\text{OHC}_{\text{ANTH}}$ , historically, averaging  $13.8 \text{ GJ m}^{-2}$  in the Arctic Ocean and  $22.4 \text{ GJ m}^{-2}$  in the Southern Ocean south of  $35^\circ\text{S}$ . The strongest historical  $\text{C}_{\text{ANTH}}$  signal,  $87 \text{ mol C m}^{-2}$ , is focused in the western North Atlantic Ocean, off the east coast of the US and Canada. The Norwegian Sea also stores particularly high historical  $\text{C}_{\text{ANTH}}$  ( $>70 \text{ mol C m}^{-2}$ ) – in good agreement with observed  $\text{C}_{\text{ANTH}}$  (Section 3.1). The equatorial global ocean and entirety of the SO generally lack historical  $\text{C}_{\text{ANTH}}$ , averaging less than  $15 \text{ mol C m}^{-2}$  each.

The responses of  $\text{OHC}_{\text{ANTH}}$  and  $\text{C}_{\text{ANTH}}$  to ice sheet melt are most disparate in the regions that are most critically important for uptake and storage. By the end of the century, AIS FW engenders a positive global  $\text{OHC}_{\text{ANTH}}$  anomaly but a negative global  $\text{C}_{\text{ANTH}}$  anomaly (Figure 3B&F). Spatially, this difference is most prevalent in the North Atlantic around the Irminger Sea where the most extreme anomalies exceed  $+4.1 \text{ GJ m}^{-2}$  ( $\text{OHC}_{\text{ANTH}}$ )

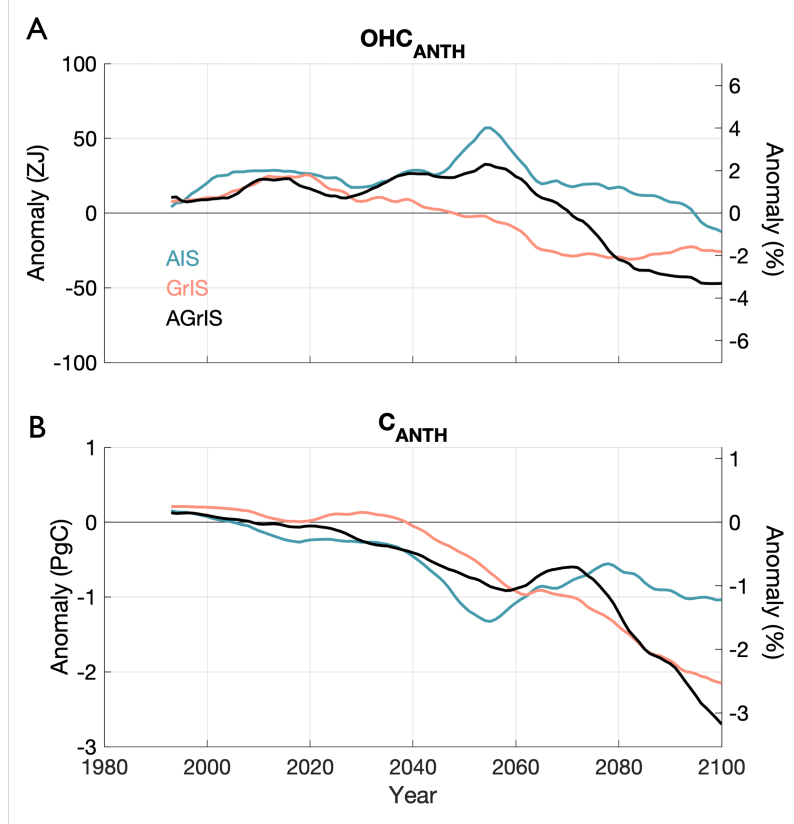


**Figure 2.** (A) Temporal evolution of global anomalous  $OHC_{ANTH}$  (10-year running mean) in the AIS (blue), GrIS (red), and AGrIS (black) simulations relative to the control simulation in ZJ on the left y-axis and in % relative to the 1992 global control  $OHC_{ANTH}$  value on the right y-axis. (B) Same as panel (A) for  $C_{ANTH}$  and in Pg C.

and  $-22.7 \text{ Pg C m}^{-2}$  ( $C_{ANTH}$ ). Similar positive (negative)  $OHC_{ANTH}$  ( $C_{ANTH}$ ) anomalies manifest in the eastern Ross Sea in the Southern Ocean (Figure 3B&F). Interestingly, the opposite response develops in the Gulf Stream as a result of AIS FW wherein the region stores anomalously more  $C_{ANTH}$  ( $+36 \text{ Pg C m}^{-2}$ ) but less  $OHC_{ANTH}$  ( $-3.1 \text{ GJ m}^{-2}$ ) in its extremes. Overall,  $OHC_{ANTH}$  and  $C_{ANTH}$  anomalies are inversely correlated in the subpolar North Atlantic, circumpolar Southern Ocean, and Gulf Stream (Figure S8).

GrIS FW causes negative global anomalies in  $OHC_{ANTH}$  and  $C_{ANTH}$  which are driven in large part by the signals in the North Atlantic, high latitude Arctic, the Atlantic sector of the Southern Ocean, and the Norwegian Sea (Figure 3C&G). Unlike the AIS simulation, GrIS FW induces negative  $OHC_{ANTH}$  responses in the subpolar North Atlantic (largest anomaly =  $-6.5 \text{ GJ m}^{-2}$ ), Equatorial and South Atlantic ( $-2.5 \text{ GJ m}^{-2}$ ), and Southern Ocean ( $-7.8 \text{ GJ m}^{-2}$ ) and positive responses in Baffin Bay ( $+4.9 \text{ GJ m}^{-2}$ ) and the Caribbean Sea ( $+3.4 \text{ GJ m}^{-2}$ ). The regional  $C_{ANTH}$  responses to GrIS and AIS FW are more similar, particularly in the North Atlantic ( $-36.9 \text{ Pg C m}^{-2}$ ) and Southern Ocean ( $-18.7 \text{ Pg C m}^{-2}$ ). The Equatorial and South Atlantic, high latitude Arctic, and Gulf Stream regions stand out as developing notably incongruous  $C_{ANTH}$  anomalies between the GrIS and AIS simulations. The spatial differences between AIS FW- and GrIS FW-induced changes mean that globally,  $OHC_{ANTH}$  and  $C_{ANTH}$  are slightly better correlated in the GrIS simulation ( $R_{GrIS,global} = 0.48$ ,  $R_{AIS,global} = 0.43$ ), but the Irminger Sea and



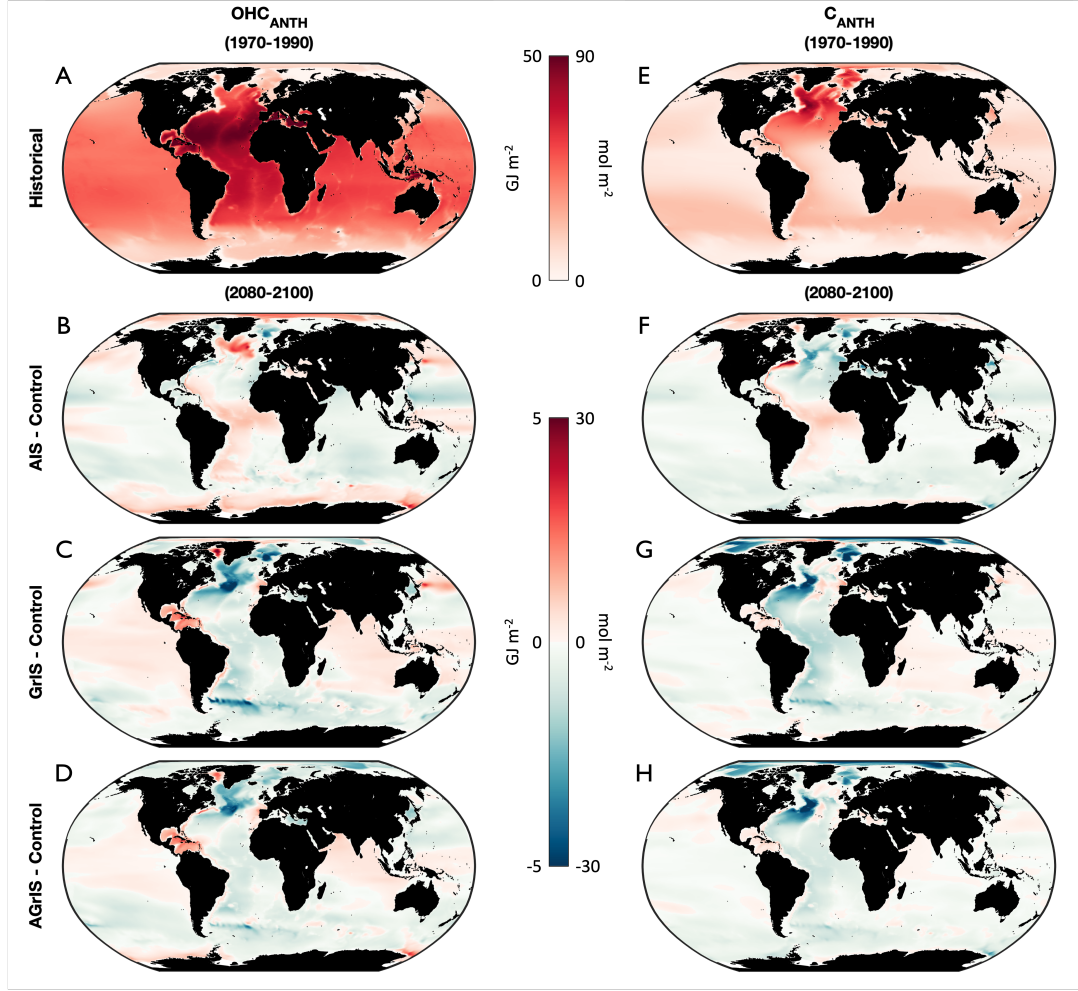


**Figure 3.** (A) Historical (1970-1990)  $OHC_{ANTH}$  in the control simulation. (B) Anomalous  $OHC_{ANTH}$  in the AIS simulation for the 2080-2100 period. (C) Same as panel (B) but for the GrIS simulation. (D) Same as panels (B-C) but for the AGrIS simulation. (E-H) Same as for panels (A-D) but for  $C_{ANTH}$ .

eastern Ross Sea still both stand out as regions where  $OHC_{ANTH}$  and  $C_{ANTH}$  anomalies are anti-correlated (Figure S8A-B).

The spatial realization of  $OHC_{ANTH}$  and  $C_{ANTH}$  anomalies in the AGrIS simulation is more similar to that of the GrIS simulation than the AIS simulation.  $OHC_{ANTH}$  and  $C_{ANTH}$  anomalies from GrIS FW develop similarly throughout much of the globe in the AGrIS simulation. Notable exceptions between the anomalous  $OHC_{ANTH}$  and  $C_{ANTH}$  responses manifest in the Norwegian Sea and high-latitude Southern Ocean where the AGrIS simulation's  $OHC_{ANTH}$  anomaly pattern is more AIS simulation-like. The  $C_{ANTH}$  spatial anomaly pattern in the AGrIS simulation is well correlated with that of the GrIS simulation, particularly throughout the Atlantic Ocean and high latitude Arctic. The AIS and AGrIS simulations produce disparate anomaly patterns in the high latitude Arctic and eastern Equatorial Atlantic (Figure S9A). The globally averaged correlation between AIS and AGrIS  $OHC_{ANTH}$  is 0.47 compared to 0.55 between the GrIS and AGrIS simulations (Figure S9A-B). For  $C_{ANTH}$ , the globally averaged AIS-AGrIS and GrIS-AGrIS correlations are 0.61 and 0.46, respectively (Figure S9C-D).

### 3.3 Contributions from linear, nonlinear, and combined ice sheet effects

The temporal evolution of global  $\text{OHC}_{\text{ANTH}}$  anomalies relative to the control simulation in response to the simultaneous freshwater discharge from the Antarctic and Greenland Ice Sheets is driven by a complex interplay of linear and nonlinear contributions from AIS and GrIS FW (Figure 4A). By the end of the century, the linear GrIS FW contribution is the largest contributor to the global  $\text{OHC}_{\text{ANTH}}$  (solid red line) but is offset by the linear AIS FW contribution (solid blue line) (Figure 4A). The largest ice-sheet FW contribution to anomalous  $\text{OHC}_{\text{ANTH}}$  at any point in the simulation period is that of the nonlinear AIS term (dashed blue line), which reaches a maximum strength of +36.1 ZJ of anomalous  $\text{OHC}_{\text{ANTH}}$  in 2055 (Figure 4A). On average from 1992 to 2055, the GrIS linear term contributes +8.9 ZJ to anomalous  $\text{OHC}_{\text{ANTH}}$  compared to the AIS linear term which contributes +25.2 ZJ averaged over the same period. The linear ice-sheet FW contributions both decrease over the course of the simulation period, which, when combined with the combined ice sheet contribution (solid grey line), drive the trend in the overall AGrIS simulation  $\text{OHC}_{\text{ANTH}}$  response (solid black line;  $d(t)$  in Equation 3). The linear GrIS contribution begins to dominate over all other terms in 2074, driving an  $\text{OHC}_{\text{ANTH}}$  anomaly of -18.2 ZJ, over 2080-2100 (Figure 4A), a 67% contribution to the -42 ZJ of anomalous global  $\text{OHC}_{\text{ANTH}}$  stored in the AGrIS simulation over this period (Figure 4B). The nonlinear AIS response further promotes the negative  $\text{OHC}_{\text{ANTH}}$  storage anomaly, contributing -11.6 ZJ – which equates to +28% of the -42 ZJ global anomaly – from 2080-2100. Together, the linear GrIS FW and nonlinear AIS FW terms contribute 95% of the total, 2080-2100  $\text{OHC}_{\text{ANTH}}$ . The other three terms in Equation 3, then, largely cancel out. The nonlinear GrIS FW contribution (+1.1 ZJ; -3%) and linear AIS contribution (+16.1, -39%) sum to an additional 17.2 ZJ taken up by the global ocean by the end of the 21<sup>st</sup> century (Figure 4B). This uptake is offset by the -19.5 ZJ  $\text{OHC}_{\text{ANTH}}$  storage anomaly induced by the combined ice sheet term.

Similar to heat, global ocean anthropogenic carbon storage exhibits a non-linear response to the simultaneous freshwater discharge from the Antarctic and Greenland Ice Sheets (Figure 4C). Beginning in the 2020s, both linear terms begin to contribute negatively to the storage of anomalous global  $\text{C}_{\text{ANTH}}$  in the AGrIS simulation (solid colored lines) combined ice sheet term (solid grey line) contributes positively after 2040 (Figure 4C). The two nonlinear terms (dashed colored lines) are fairly negligible throughout the simulation (Figure 4C). Averaged from 2080-2100, the global ocean in the AGrIS simulation stores 2 Pg C less than in the control simulation and is mostly driven by the linear GrIS FW effects (Figure 4D). As with  $\text{OHC}_{\text{ANTH}}$ , the linear GrIS term is the largest contributor to global  $\text{C}_{\text{ANTH}}$  in the AGrIS simulation at -1.6 Pg C (80%) over the 2080-2100 period (solid red bar in Figure 4D). The linear AIS FW response enhances that of GrIS FW, contributing -1.1 Pg C (52%) to the total  $\text{C}_{\text{ANTH}}$  storage anomaly (Figure 4D). While relatively important for  $\text{OHC}_{\text{ANTH}}$  storage, the nonlinear AIS FW effects are the least important for  $\text{C}_{\text{ANTH}}$ , contributing +0.1 (-7%) to the global anomaly (Figure 4D). Like the AIS nonlinear term, the GrIS nonlinear term is also fairly weak (-0.3 Pg C; 13%) compared to its linear counterpart by the end of the simulation (2080-2100; Figure 4D). While the global  $\text{C}_{\text{ANTH}}$  anomaly in the AGrIS simulation is dominated by the two linear, single ice sheet terms ( $\text{AIS}_{\text{linear}}$  and  $\text{GrIS}_{\text{linear}}$ ), their cumulative -2.7 Pg storage anomaly is dampened by the combined ice sheet effects (Figure 4D). The combined ice sheet FW fluxes result in a +0.8 Pg  $\text{C}_{\text{ANTH}}$  storage anomaly which constitutes a -38% contribution to the global  $\text{C}_{\text{ANTH}}$  response (Figure 4D).

#### 3.3.1 Response Predictors

The two most important variable in predicting ice sheet-driven changes are identical for both  $\text{OHC}_{\text{ANTH}}$  and  $\text{C}_{\text{ANTH}}$  (Figure 5). When systematically removing one predictor and rerunning the GPR model for each of the five predictor variables (AMOC, SSS, SST,  $\text{SIE}_{\text{NH}}$ , and  $\text{SIE}_{\text{SH}}$ ), SSS produces the highest RMSE values for both  $\text{OHC}_{\text{ANTH}}$

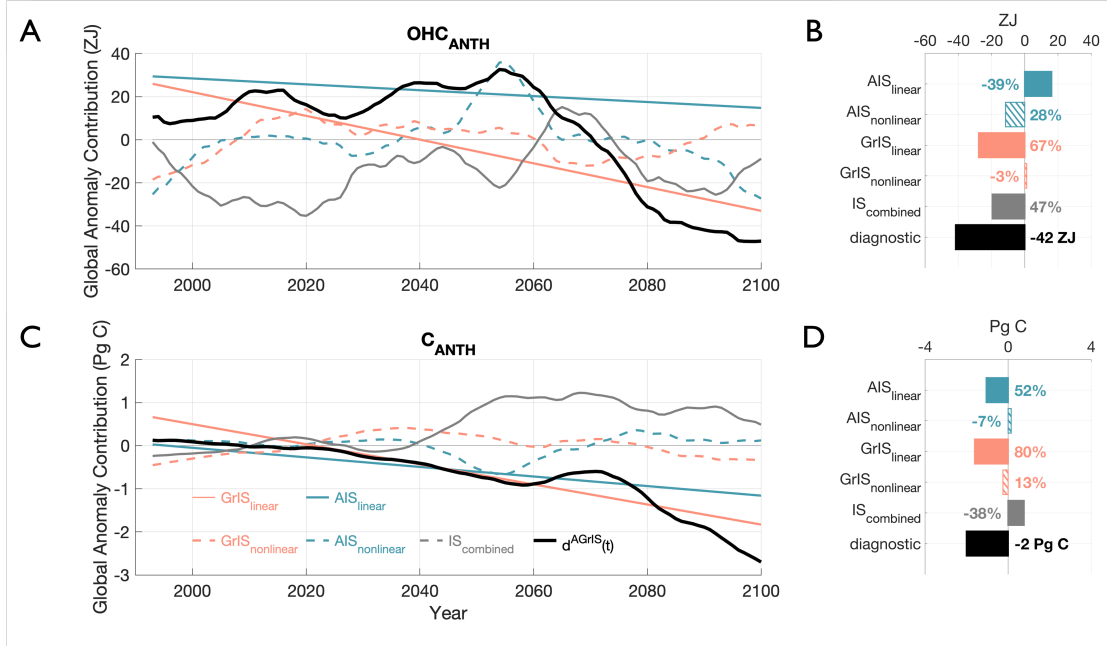


**Figure 4.** (A) Temporal evolution of each term in equation 3 using column-integrated  $OHC_{ANTH}$  as the diagnostic. Solid and dashed lines show the linear and nonlinear contributions to the global  $OHC_{ANTH}$  and  $C_{ANTH}$  anomalies resulting from AIS (blue) and GrIS (red) freshwater, respectively. Grey and black lines show the combined ice sheet effects and global, column-integrated diagnostic response, respectively. (B) Contributions from each term in panel (A) from 2080-2100. Solid and hatch filled bars show the linear and nonlinear contributions from the AIS (blue) and GrIS (red). Percentages denote the relative contribution of each term to the global  $OHC_{ANTH}$  anomaly averaged over the 2080-2100 period. The global  $OHC_{ANTH}$  anomaly in ZJ from 2080-2100 is printed in black. (C-D) Same as panels (A-B) but for  $C_{ANTH}$  and in Pg C.

and  $C_{ANTH}$  for all four simulations, establishing SSS as the predominant predictor for the GPR model's predictions. For  $OHC_{ANTH}$ , normalized RMSE values when withholding SSS range from 0.025 to 0.026 across model experiments compared to 0.023 to 0.029 for  $C_{ANTH}$  (Table S4). The next most important predictor is SST with normalized RMSE values averaging to 0.020 across simulations for both diagnostics. AMOC,  $SIE_{NH}$ , and  $SIE_{SH}$ , respectively, follow in importance for  $OHC_{ANTH}$  and are all more variable across simulations than either SSS or SST (Figure 5A, Table S4). For  $C_{ANTH}$ ,  $SIE_{NH}$  and  $SIE_{SH}$  are the next two most important predictors with approximately equal normalized RMSE averages followed lastly by AMOC (Figure 5B, Table S4).

### 3.4 Timing and depth-distribution of combined ice sheet effects

Ice sheet-driven changes in global ocean heat content propagate more quickly from surface to depth than ice sheet-driven changes in anthropogenic carbon (Figure 6). Surface changes in the combined ice sheet effects on  $OHC_{ANTH}$  first become apparent at depth within the first 30 years of simulation time (Figure 6A). Considering  $OHC_{ANTH}$  in the upper ocean (surface - 700 m), the strength of the combined ice sheet term peaks in 2058 at 74 ZJ. The magnitude of the combined ice sheet effects on middle (700 m - 2000 m) and lower (2000 m - bottom) ocean layers also reach maxima in the middle decades of the 21<sup>st</sup> century at +17 ZJ in 2050 (middle) and -30 ZJ in 2037 (lower; Figure 6A). In contrast, the combined ice sheet impacts are not realized until after 2070 for  $C_{ANTH}$  for

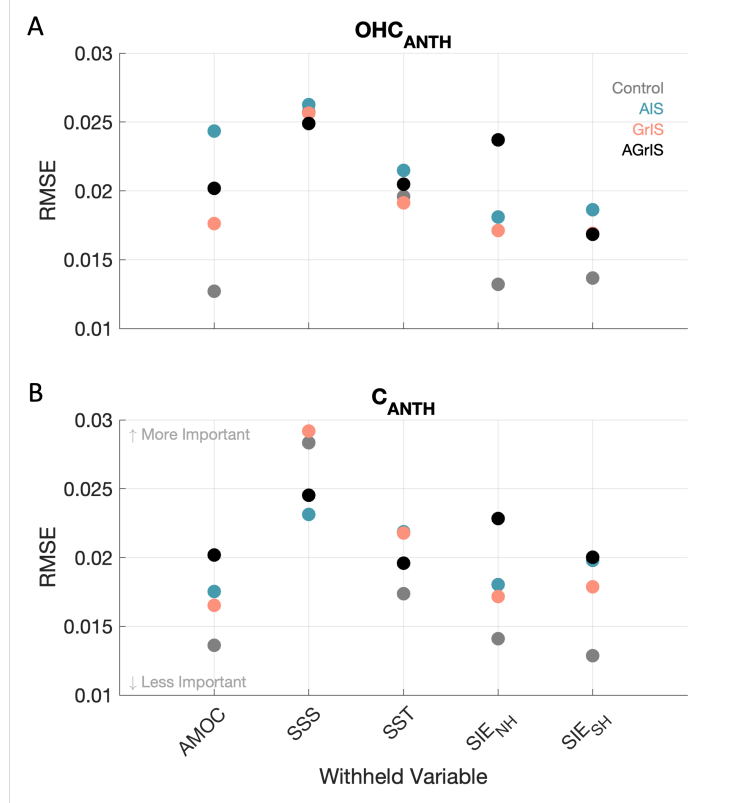


**Figure 5.** (A) Root Mean Square Error (RMSE) values between the Gaussian Predictor Response (GPR) predicted  $OHC_{ANTH}$  and actual  $OHC_{ANTH}$  generated by withholding one predictor at a time for the Control (grey), AIS (blue), GrIS (pink), and AGrIS (black) simulations.

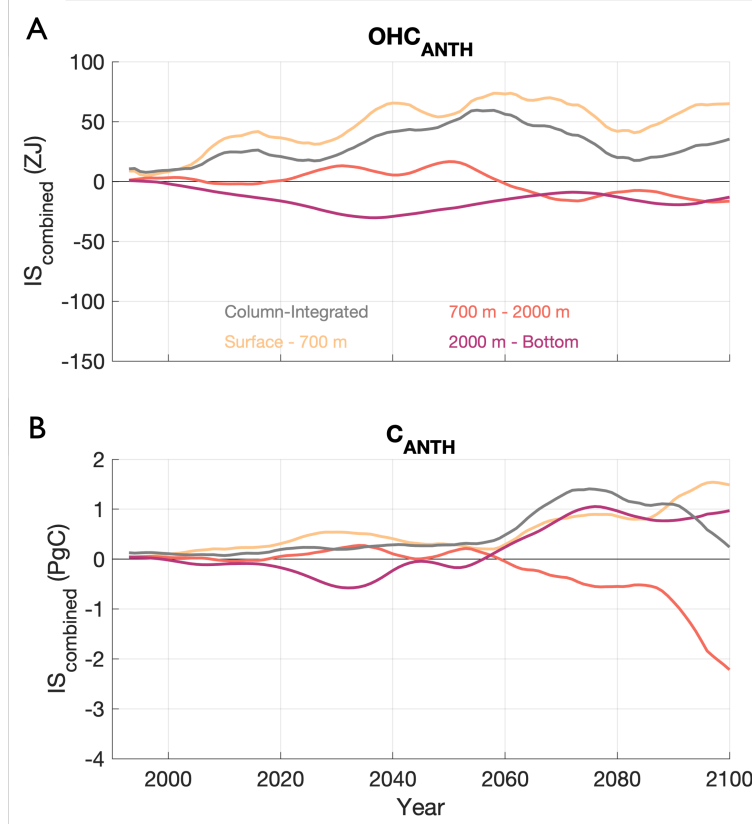


**Figure 6.** (A) Temporal evolution of the  $IS_{combined}$  term (see Equation 3) for  $OHC_{ANTH}$  for the surface - 700 m depth (yellow), 700 m - 2000 m depth (orange), 2000 m - bottom (pink), and integrated over the whole water column (grey). (B) Same as panel (A) but for  $C_{ANTH}$ .

all depth levels (Figure 6B). The magnitude of combined ice sheet effects on  $C_{ANTH}$  in the upper, middle, and lower ocean layers peak in 2097, 2100, and 2076 at 1.5 Pg C, -2.2 Pg C, and 1.0 Pg C, respectively. From 2080-2100, the largest  $OHC_{ANTH}$  anomalies from combined ice sheet effects manifest in the upper ocean layer (+54 ZJ) while largest  $C_{ANTH}$  anomalies manifest in the middle ocean layer (-1.1 Pg C). Furthermore, the lower ocean layer stores anomalously less  $OHC_{ANTH}$  (-17 ZJ) but more  $C_{ANTH}$  (+0.8 Pg C) than the control over the same 2080-2100 period. In both, however, the net impacts from integrating over the column are such that the combined ice sheet contributions are positive by 2100 (Figure 6).

#### 4 Discussion and Conclusions

We leverage a state-of-the-art GCM experiment with comparably applied AIS and GrIS FW forcings to directly contrast the  $OHC_{ANTH}$  and  $C_{ANTH}$  impacts generated by each ice sheet's projected mass changes. We offer new perspective on quantifying the linear and nonlinear contributions to  $OHC_{ANTH}$  and  $C_{ANTH}$  due to FW from each ice sheet separately and from both ice sheets combined. By the end of the 21<sup>st</sup> century, the combined effect of both ice sheets is an anomalous reduction in both  $OHC_{ANTH}$  and  $C_{ANTH}$  storage in the global ocean. The global  $OHC_{ANTH}$  anomaly in the combined ice sheet scenario generally follows the positive trend of the AIS simulation through the first half of the 21<sup>st</sup> century and the negative trend of the GrIS simulation through the second half. Freshwater discharge from each individual ice sheet induces a negative  $C_{ANTH}$  trend, and

the combined ice sheet response follows the positive trend response realized in the AIS simulation more closely through roughly 2050 and the GrIS simulation thereafter. The high-latitude North Atlantic and Southern Ocean – important regions for historical anthropogenic heat and carbon storage and fluxes (Gruber et al., 2002, 2019; Bronselaer et al., 2020; Huguenin et al., 2022) – develop disparate anomalous  $\text{OHC}_{\text{ANTH}}$  and  $\text{C}_{\text{ANTH}}$  responses to ice sheet FW. Anomalies in both global  $\text{OHC}_{\text{ANTH}}$  and  $\text{C}_{\text{ANTH}}$  respond non-linearly to simultaneous ice sheet freshwater discharge though the linear response to GrIS FW dominates both signals. Despite distinct realizations, SSS is the preeminent driver of global, ice sheet-induced changes to both  $\text{OHC}_{\text{ANTH}}$  and  $\text{C}_{\text{ANTH}}$ . Manifesting disparately in both depth and time, global  $\text{OHC}_{\text{ANTH}}$  anomalies develop more quickly than global  $\text{C}_{\text{ANTH}}$  anomalies.

Stemming from distinct historical storage, disparate  $\text{OHC}_{\text{ANTH}}$  and  $\text{C}_{\text{ANTH}}$  changes are further accentuated by their divergent responses to ice sheet FW. As a region of markedly high uptake for both  $\text{OHC}_{\text{ANTH}}$  and  $\text{C}_{\text{ANTH}}$ , contrasting responses in the high-latitude North Atlantic demonstrate that changes to one diagnostic do not necessarily directly correspond to changes in the other. Bronselaer et al. (2020) also explore the future relationship of  $\text{OHC}_{\text{ANTH}}$  and  $\text{C}_{\text{ANTH}}$  resulting from changing atmospheric conditions. Instead of directly investigating changing FW fluxes from ice sheets, they analyze output from two comparable simulations: one that regulates ocean currents to that of the pre-industrial state and another that is allowed to evolve freely under transient,  $1\% \text{ y}^{-1}$  increase in anthropogenic carbon (Bronselaer et al., 2020). In their study, they find a linear relationship between the global ocean  $\text{OHC}_{\text{ANTH}}$  and  $\text{C}_{\text{ANTH}}$  uptake due to anthropogenic changes (Bronselaer et al., 2020). In contrast, our results explore the anomalous changes to these global inventories owing solely to differences stemming from increasing freshwater fluxes from the Antarctic and Greenland Ice Sheets.

The reduced  $\text{C}_{\text{ANTH}}$  signal in the AGrIS simulation – driven by GrIS FW – indicates that the high latitude North Atlantic, and, thus, the global ocean, will do less to mitigate rising atmospheric carbon levels over the coming century. The global  $\text{C}_{\text{ANTH}}$  anomaly in the AGrIS simulation ( $-2.09 \text{ Pg C}$ ) represents a 2.5% change to the global  $\text{C}_{\text{ANTH}}$  inventory in the control simulation in 1992 ( $\sim 0.5\%$  of the total inventory in 2100). Per Bindoff et al. (2007), the global ocean has absorbed a majority of  $\text{OHC}_{\text{ANTH}}$  in the past half century. Weakening the ocean’s ability to store additional  $\text{C}_{\text{ANTH}}$  will lead to elevated atmospheric  $\text{CO}_2$  concentrations by the end of the 21<sup>st</sup> century. The global ocean buffering capacity for increasing atmospheric temperatures is also diminished ( $-3\%$ ) as a result of combined ice sheet FW fluxes – particularly in the North Atlantic, a region that helps govern global  $\text{OHC}_{\text{ANTH}}$  trends (Gruber et al., 2002; Huguenin et al., 2022). In constellation, positive and negative global storage anomalies in the upper ocean (0 m - 700 m) and middle ocean (700 m - 2000 m), respectively, indicate that less  $\text{OHC}_{\text{ANTH}}$  and  $\text{C}_{\text{ANTH}}$  are being transported to depth; instead accumulating in the surface layer. The relatively small difference in global  $\text{C}_{\text{ANTH}}$  storage indicates that the strength of the warming scenario is a significantly stronger driver of anthropogenic carbon in the ocean than ice sheet runoff. As such, it is plausible that these results would be exacerbated under stronger warming conditions and/or over a longer investigation period. Thus, as the surface ocean stores more  $\text{OHC}_{\text{ANTH}}$  and  $\text{C}_{\text{ANTH}}$  under this strong atmospheric warming, it is less capable of taking up more (Maier-Reimer & Hasselmann, 1987; Gruber et al., 2023), indicating a further reduction in uptake efficacy for both parameters beyond 2100.

The effects of singular ice sheet freshwater discharge on anthropogenic ocean heat and carbon storage do not linearly combine to produce the effects of simultaneous ice sheet freshwater discharge. To project realistic FW-induced changes, simulating both ice sheets simultaneously is thus imperative. Linearly summing the globally averaged anomalies from the AIS and GrIS simulations leads to an underestimation of anomalous  $\text{OHC}_{\text{ANTH}}$  storage (30.0 ZJ) and an overestimation of  $\text{C}_{\text{ANTH}}$  storage (2.66 Pg C) when compared



to the AGrIS simulation. As modeling centers move toward incorporating active ice sheet components into their GCMs, first focusing on representing increasing GrIS FW fluxes is critical for estimating the projected the global and regional FW-induced changes to both  $\text{OHC}_{\text{ANTH}}$  and  $\text{C}_{\text{ANTH}}$ . However, AIS FW impacts are still robust enough to affect the global  $\text{OHC}_{\text{ANTH}}$  and  $\text{C}_{\text{ANTH}}$  inventories, the eventual inclusion of an active AIS is also imperative for getting an accurate assessment of these changes. Because these AIS FW impacts manifest later than those from GrIS FW, shorter simulations will indicate higher GrIS dependence in the evolution of global  $\text{OHC}_{\text{ANTH}}$  and  $\text{C}_{\text{ANTH}}$ . Li, Marshall, et al. (2023), who use linear convolution theory to disentangle linear and nonlinear responses, find the AIS FW causes a stronger response in air temperature, sea ice extent and deep-water formation and that these responses only become nonlinear after exceeding a  $5000 \text{ Gt y}^{-1}$  melt rate threshold. Instead of a slow ramp up of FW discharge, Li, Marshall, et al. (2023) apply a step-wise increase of FW from  $0 \text{ Gt y}^{-1}$  to  $500 \text{ Gt y}^{-1}$ ,  $2000 \text{ Gt y}^{-1}$ , and  $5000 \text{ Gt y}^{-1}$  for each individual ice sheet as well as their combined ice sheet simulation. Unlike their experiment, we gradually increase spatially heterogeneous ice sheet FW fluxes and find that the GrIS rather than the AIS dominates anomalous changes through the 21<sup>st</sup> century. Moreover, we find that the ice sheets' nonlinear impacts on  $\text{OHC}_{\text{ANTH}}$  and  $\text{C}_{\text{ANTH}}$  anomalies begin to manifest in the 2050s, well before FW fluxes from either ice sheet exceed  $5000 \text{ Gt y}^{-1}$ . That said, due to the longer time-scale of the realization of AIS FW impacts, longer simulations will be necessary to fully quantify the cumulative AIS FW impacts as the AIS becomes an active component in GCMs.

The major caveats of this work include the approach to projecting future FW fluxes and the application of those FW fluxes to the surrounding ocean grid cells. Our AIS FW forcings assume that past spatial patterns of mass loss and solid-to-liquid flux ratios will continue into the future. Our observational record of mass change for both ice sheets extends back only  $\sim 20$  years, restricting our ability to assess both ice sheet-integrated and spatially resolved decadal and interdecadal trends. Supplementing these data with information from ice sheet models indicates that past WAIS mass loss is projected to not only continue, but intensify in the future (Rignot et al., 2019). The future AIS-integrated FW forcing lacks important climate feedback as it subsumes output generated by a model without an active AIS component. Future GrIS FW fluxes are based on active Greenland CESM2 model output simulated under SSP5-8.5 atmospheric forcing. The AIS FW flux values are predicated upon the assumption of ice shelf mass balance which we made for two reasons: (1) the GRACE satellites do not measure mass changes of the ice shelves and (2) CESM2 currently lacks the ability to model floating ice shelves. The former reason means that we have little information to guide any ice shelf mass imbalances and the latter reason means that, even if we did have ice shelf mass imbalance estimates, we are not yet able to simulate them in CESM2. As a result, we assume the ice shelves are in mass balance and that mass changes to the grounded AIS are realized immediately as FW fluxes into the surrounding ocean. Finally, as these FW fluxes (modeled as salinity fluxes with no information on temperature or momentum) are distributed into the surrounding ocean, we apply them directly to the surface coastal grid cells. Realistically, calved ice distributes FW solely to the surface ocean but is spread further offshore as it is carried via ocean currents while basal melt is distributed horizontally across the underside of the ice shelves, at depths exceeding 1 km (Dinniman et al., 2016). Another limitation of this work is the use of a single ensemble member for each simulation meaning we lack the ability to fully assess the role of internal variability.

Despite these limitations, our findings underscore the need for further exploration of ice sheet FW impacts on global anthropogenic heat and carbon storage. The AIS and GrIS engender distinct responses for global  $\text{OHC}_{\text{ANTH}}$  and global  $\text{C}_{\text{ANTH}}$  anomalies and their impacts cannot simply be linearly added to capture their combined effects. As the polar regions are uniquely important for heat and carbon uptake, actively modeling the

ice sheets and incorporating feedbacks induced by their melt will impact projections of the ocean's capacity to mitigate rising atmospheric carbon and heat.

## 5 Open Research

Data from the CONTROL simulation presented in this paper are publicly available at Gorte et al. (2024e) (historical) and Gorte et al. (2024f) (2015-2100). Data from the AIS simulation presented in this paper are publicly available at Gorte et al. (2024c) (historical) and Gorte et al. (2024d) (2015-2100). Data from the GrIS simulation presented in this paper are publicly available at Gorte et al. (2024g) (historical) and Gorte et al. (2024h) (2015-2100). Data from the AGrIS simulation presented in this paper are publicly available at Gorte et al. (2024a) (historical) and Gorte et al. (2024b) (2015-2100).

## Acknowledgments

We would like to thank Dr. Leo van Kampenhout for his work in the setup of these experiments. This work was performed at the University of Colorado Boulder and Institute of Arctic and Alpine Research and was supported by the NASA's Sea Level Change Team (award #80NSSC20K1123). NSL and CN are grateful for funding from the U.S. Department of Energy (DE-SC0022243). We would also like to acknowledge NCAR's Land Ice and Polar Climate Working Groups for their valuable computing time contributions.

## References

- Abraham, J., Cheng, L., Mann, M. E., Trenberth, K., & von Schuckmann, K. (2022). The ocean response to climate change guides both adaptation and mitigation efforts. *Atmospheric and Oceanic Science Letters*, 15, 100221. Retrieved from <https://www.sciencedirect.com/science/article/pii/S1674283422000964> doi: <https://doi.org/10.1016/j.aosl.2022.100221>
- Abraham, J. P., Baringer, M., Bindoff, N. L., Boyer, T., Cheng, L. J., Church, J. A., ... Willis, J. K. (2013). A review of global ocean temperature observations: Implications for ocean heat content estimates and climate change. *Reviews of Geophysics*, 51, 450-483. Retrieved from <https://agupubs.onlinelibrary.wiley.com/doi/abs/10.1002/rog.20022> doi: <https://doi.org/10.1002/rog.20022>
- Bindoff, N., Willebrand, J., Artale, V., Cazenave, A., Gregory, J., Gulev, S., ... others (2007). Climate change 2007: The physical science basis. contribution of working group i to the fourth assessment report of the intergovernmental panel on climate change. *Solomon, S.; Qin, D.;*
- Bintanja, R., & Oerlemans, J. (1995, 8). The influence of the albedo-temperature feedback on climate sensitivity. *Annals of Glaciology*, 21. doi: 10.1017/S0260305500016062
- Bintanja, R., Oldenborgh, G. J. V., Drijfhout, S. S., Wouters, B., & Katsman, C. A. (2013, 5). Important role for ocean warming and increased ice-shelf melt in antarctic sea-ice expansion. *Nature Geoscience*, 6, 376-379. doi: 10.1038/NGEO1767
- Bronselaer, B., Russell, J. L., Winton, M., Williams, N. L., Key, R. M., Dunne, J. P., ... Sarmiento, J. L. (2020, 1). Importance of wind and meltwater for observed chemical and physical changes in the southern ocean. *Nature Geoscience*, 13, 35-42. doi: 10.1038/s41561-019-0502-8
- Bronselaer, B., Winton, M., Griffies, S. M., Hurlin, W. J., Rodgers, K. B., Sergienko, O. V., ... Russell, J. L. (2018, 11). Change in future climate due to antarctic meltwater. *Nature* 2018 564:7734, 564, 53-58. doi: 10.1038/s41586-018-0712-z
- Cheng, L., Abraham, J., Trenberth, K. E., Fasullo, J., Boyer, T., Locarnini, R., ...

- Zhu, J. (2021). Upper ocean temperatures hit record high in 2020. *Advances in Atmospheric Sciences*, 38, 523-530. Retrieved from <https://doi.org/10.1007/s00376-021-0447-x> doi: 10.1007/s00376-021-0447-x
- Cheng, L., von Schuckmann, K., Abraham, J. P., Trenberth, K. E., Mann, M. E., Zanna, L., ... Lin, X. (2022). Past and future ocean warming. *Nature Reviews Earth Environment*, 3, 776-794. Retrieved from <https://doi.org/10.1038/s43017-022-00345-1> doi: 10.1038/s43017-022-00345-1
- Crook, J. A., Forster, P. M., & Stuber, N. (2011). Spatial patterns of modeled climate feedback and contributions to temperature response and polar amplification. *Journal of Climate*, 24, 3575 - 3592. Retrieved from <https://journals.ametsoc.org/view/journals/clim/24/14/2011jcli3863.1.xml> doi: <https://doi.org/10.1175/2011JCLI3863.1>
- Danabasoglu, G., Lamarque, J. F., Bacmeister, J., Bailey, D. A., DuVivier, A. K., Edwards, J., ... Strand, W. G. (2020, 2). The community earth system model version 2 (cesm2). *Journal of Advances in Modeling Earth Systems*, 12, e2019MS001916. Retrieved from <https://onlinelibrary.wiley.com/doi/full/10.1029/2019MS001916> <https://onlinelibrary.wiley.com/doi/abs/10.1029/2019MS001916> <https://agupubs.onlinelibrary.wiley.com/doi/10.1029/2019MS001916> doi: 10.1029/2019MS001916
- Davila, X., Gebbie, G., Brakstad, A., Lauvset, S. K., McDonagh, E. L., Schwinger, J., & Olsen, A. (2022). How is the ocean anthropogenic carbon reservoir filled? *Global Biogeochemical Cycles*, 36, e2021GB007055. Retrieved from <https://agupubs.onlinelibrary.wiley.com/doi/abs/10.1029/2021GB007055> (e2021GB007055 2021GB007055) doi: <https://doi.org/10.1029/2021GB007055>
- DeConto, R. M., & Pollard, D. (2016, 3). Contribution of antarctica to past and future sea-level rise. *Nature*, 531, 591-597. doi: 10.1038/nature17145
- DeConto, R. M., Pollard, D., Alley, R. B., Velicogna, I., Gasson, E., Gomez, N., ... Dutton, A. (2021, 5). The paris climate agreement and future sea-level rise from antarctica. *Nature* 2021 593:7857, 593, 83-89. Retrieved from <https://www.nature.com/articles/s41586-021-03427-0> doi: 10.1038/s41586-021-03427-0
- DeVries, T., Yamamoto, K., Wanninkhof, R., Gruber, N., Hauck, J., Müller, J. D., ... Zeng, J. (2023). Magnitude, trends, and variability of the global ocean carbon sink from 1985-2018. *Global Biogeochemical Cycles*(1). doi: 10.1029/2023GB007780
- Dinniman, M. S., Asay-Davis, X. S., Galton-Fenzi, B. K., Holland, P. R., Jenkins, A., & Timmermann, R. (2016, December). Modeling ice shelf/ocean interaction in antarctica: A review. *Oceanography, issue volume*. Retrieved from <https://doi.org/10.5670/oceanog.2016.106> (The most rapid loss of ice from the Antarctic Ice Sheet is observed where ice streams flow into the ocean and begin to float, forming the great Antarctic ice shelves that surround much of the continent. Because these ice shelves are floating, their thinning does not greatly influence sea level. However, they also buttress the ice streams draining the ice sheet, and so ice shelf changes do significantly influence sea level by altering the discharge of grounded ice. Currently, the most significant loss of mass from the ice shelves is from melting at the base (although iceberg calving is a close second). Accessing the ocean beneath ice shelves is extremely difficult, so numerical models are invaluable for understanding the processes governing basal melting. This paper describes the different ways in which ice shelf/ocean interactions are modeled and discusses emerging directions that will enhance understanding of how the ice shelves are melting now and how this might change in the future.)
- Fletcher, S. E. M., Gruber, N., Jacobson, A. R., Doney, S. C., Dutkiewicz, S., Gerber, M., ... Sarmiento, J. L. (2006). Inverse estimates of anthropogenic co2

- uptake, transport, and storage by the ocean. *Global Biogeochemical Cycles*, 20. Retrieved from <https://agupubs.onlinelibrary.wiley.com/doi/abs/10.1029/2005GB002530> doi: <https://doi.org/10.1029/2005GB002530>
- Friedlingstein, P., O'Sullivan, M., Jones, M. W., Andrew, R. M., Gregor, L., Hauck, J., ... Zheng, B. (2022). Global carbon budget 2022. *Earth System Science Data*, 14, 4811-4900. Retrieved from <https://essd.copernicus.org/articles/14/4811/2022/> doi: 10.5194/essd-14-4811-2022
- Frölicher, T. L., Sarmiento, J. L., Paynter, D. J., Dunne, J. P., Krasting, J. P., & Winton, M. (2015). Dominance of the southern ocean in anthropogenic carbon and heat uptake in cmip5 models. *Journal of Climate*, 28, 862-886. doi: 10.1175/JCLI-D-14-00117.1
- Goelzer, H., Nowicki, S., Payne, A., Larour, E., Seroussi, H., Lipscomb, W. H., ... van den Broeke, M. (2020). The future sea-level contribution of the greenland ice sheet: a multi-model ensemble study of ismip6. *The Cryosphere*, 14, 3071-3096. Retrieved from <https://tc.copernicus.org/articles/14/3071/2020/> doi: 10.5194/tc-14-3071-2020
- Goosse, H., Kay, J. E., Armour, K. C., Bodas-Salcedo, A., Chepfer, H., Docquier, D., ... Vancoppenolle, M. (2018). Quantifying climate feedbacks in polar regions. *Nature Communications*, 9, 1919. Retrieved from <https://doi.org/10.1038/s41467-018-04173-0> doi: 10.1038/s41467-018-04173-0
- Gorte, T., Lovenduski, N. S., Nissen, C., Lenaerts, J., & Weiss, J. (2024a, 1). *Cesm2 agris simulation output (1992-2014): The nonlinear and distinct responses of ocean heat content and anthropogenic carbon to ice sheet freshwater discharge in a warming climate*. Zenodo. Retrieved from <https://doi.org/10.5281/zenodo.10443828> doi: 10.5281/zenodo.10443828
- Gorte, T., Lovenduski, N. S., Nissen, C., Lenaerts, J., & Weiss, J. (2024b, 1). *Cesm2 agris simulation output (2015-2100): The nonlinear and distinct responses of ocean heat content and anthropogenic carbon to ice sheet freshwater discharge in a warming climate*. Zenodo. Retrieved from <https://doi.org/10.5281/zenodo.10447519> doi: 10.5281/zenodo.10447519
- Gorte, T., Lovenduski, N. S., Nissen, C., Lenaerts, J., & Weiss, J. (2024c, 1). *Cesm2 ais simulation output (1992-2014): The nonlinear and distinct responses of ocean heat content and anthropogenic carbon to ice sheet freshwater discharge in a warming climate*. Zenodo. Retrieved from <https://doi.org/10.5281/zenodo.10433209> doi: 10.5281/zenodo.10433209
- Gorte, T., Lovenduski, N. S., Nissen, C., Lenaerts, J., & Weiss, J. (2024d, 1). *Cesm2 ais simulation output (2015-2100): The nonlinear and distinct responses of ocean heat content and anthropogenic carbon to ice sheet freshwater discharge in a warming climate*. Zenodo. Retrieved from <https://doi.org/10.5281/zenodo.10433336> doi: 10.5281/zenodo.10433336
- Gorte, T., Lovenduski, N. S., Nissen, C., Lenaerts, J., & Weiss, J. (2024e, 1). *Cesm2 control simulation output (1970-2014): The nonlinear and distinct responses of ocean heat content and anthropogenic carbon to ice sheet freshwater discharge in a warming climate*. Zenodo. Retrieved from <https://doi.org/10.5281/zenodo.10419440> doi: 10.5281/zenodo.10419440
- Gorte, T., Lovenduski, N. S., Nissen, C., Lenaerts, J., & Weiss, J. (2024f, 1). *Cesm2 control simulation output (2015-2100): The nonlinear and distinct responses of ocean heat content and anthropogenic carbon to ice sheet freshwater discharge in a warming climate*. Zenodo. Retrieved from <https://doi.org/10.5281/zenodo.10429589> doi: 10.5281/zenodo.10429589
- Gorte, T., Lovenduski, N. S., Nissen, C., Lenaerts, J., & Weiss, J. (2024g, 1). *Cesm2 gris simulation output (1992-2014): The nonlinear and distinct responses of ocean heat content and anthropogenic carbon to ice sheet freshwater discharge in a warming climate*. Zenodo. Retrieved from <https://doi.org/10.5281/zenodo.10439532> doi: 10.5281/zenodo.10439532

- Gorte, T., Lovenduski, N. S., Nissen, C., Lenaerts, J., & Weiss, J. (2024h, 1). *Cesm2 gris simulation output (2015-2100): The nonlinear and distinct responses of ocean heat content and anthropogenic carbon to ice sheet freshwater discharge in a warming climate*. Zenodo. Retrieved from <https://doi.org/10.5281/zenodo.10433919> doi: 10.5281/zenodo.10433919
- Gorte, T., Lovenduski, N. S., Nissen, C., & Lenaerts, J. T. M. (2023, 6). Antarctic ice sheet freshwater discharge drives substantial southern ocean changes over the 21<sup>st</sup> century. Retrieved from <https://doi.org/10.22541/2Fessoar.168771427.74160260%2Fv1> doi: 10.22541/essoar.168771427.74160260/v1
- Gruber, N., Bakker, D. C. E., DeVries, T., Gregor, L., Hauck, J., Landschützer, P., ... Müller, J. D. (2023). Trends and variability in the ocean carbon sink. *Nature Reviews Earth Environment*, 4, 119-134. Retrieved from <https://doi.org/10.1038/s43017-022-00381-x> doi: 10.1038/s43017-022-00381-x
- Gruber, N., Clement, D., Carter, B. R., Feely, R. A., van Heuven, S., Hoppema, M., ... Wanninkhof, R. (2019). The oceanic sink for anthropogenic  $\text{CO}_2$  from 1994 to 2007. *Science*, 363, 1193-1199. Retrieved from <https://www.science.org/doi/abs/10.1126/science.aau5153> doi: 10.1126/science.aau5153
- Gruber, N., Keeling, C. D., & Bates, N. R. (2002). Interannual variability in the north atlantic ocean carbon sink. *Science*, 298, 2374-2378. Retrieved from <https://www.science.org/doi/abs/10.1126/science.1077077> doi: 10.1126/science.1077077
- Holland, M. M., & Bitz, C. M. (2003). Polar amplification of climate change in coupled models. *Climate Dynamics*, 21, 221-232. Retrieved from <https://doi.org/10.1007/s00382-003-0332-6> doi: 10.1007/s00382-003-0332-6
- Huguenin, M. F., Holmes, R. M., & England, M. H. (2022). Drivers and distribution of global ocean heat uptake over the last half century. *Nature Communications*, 13, 4921. Retrieved from <https://doi.org/10.1038/s41467-022-32540-5> doi: 10.1038/s41467-022-32540-5
- Khatiwala, S., Tanhua, T., Fletcher, S. M., Gerber, M., Doney, S. C., Graven, H. D., ... Sabine, C. L. (2013). Global ocean storage of anthropogenic carbon. *Biogeosciences*, 10, 2169-2191. doi: 10.5194/bg-10-2169-2013
- Lenaerts, J. T., Medley, B., van den Broeke, M. R., & Wouters, B. (2019). Observing and modeling ice sheet surface mass balance. *Reviews of Geophysics*. doi: 10.1029/2018RG000622
- Lenaerts, J. T. M., Bars, D. L., van Kampenhout, L., Vizcaino, M., Enderlin, E. M., & van den Broeke, M. R. (2015, 8). Representing greenland ice sheet freshwater fluxes in climate models. *Geophysical Research Letters*, 42, 6373-6381. Retrieved from <http://doi.wiley.com/10.1002/2015GL064738> doi: 10.1002/2015GL064738
- Li, Q., England, M. H., Hogg, A. M., Rintoul, S. R., & Morrison, A. K. (2023, 3). Abyssal ocean overturning slowdown and warming driven by antarctic meltwater. *Nature*, 615, 841-847. Retrieved from <https://www.nature.com/articles/s41586-023-05762-w> doi: 10.1038/s41586-023-05762-w
- Li, Q., Marshall, J., Rye, C. D., Romanou, A., Rind, D., & Kelley, M. (2023). Global climate impacts of greenland and antarctic meltwater: A comparative study. *J. Climate*, 36(11), 3571-3590. doi: 10.1175/JCLI-D-22-0433.1
- Long, M. C., Stephens, B. B., McKain, K., Sweeney, C., Keeling, R. F., Kort, E. A., ... Wofsy, S. C. (2021). Strong southern ocean carbon uptake evident in airborne observations. *Science*, 374, 1275-1280. Retrieved from <https://www.science.org/doi/abs/10.1126/science.abi4355> doi: 10.1126/science.abi4355
- Maier-Reimer, E., & Hasselmann, K. (1987). Transport and storage of  $\text{CO}_2$  in the ocean —an inorganic ocean-circulation carbon cycle model. *Climate Dynamics*, 2, 63-90. Retrieved from <https://doi.org/10.1007/BF01054491> doi: 10



- .1007/BF01054491
- Manabe, S., & Stouffer, R. J. (1980). Sensitivity of a global climate model to an increase of co<sub>2</sub> concentration in the atmosphere. *Journal of Geophysical Research: Oceans*, 85, 5529-5554. Retrieved from <https://agupubs.onlinelibrary.wiley.com/doi/abs/10.1029/JC085iC10p05529> doi: <https://doi.org/10.1029/JC085iC10p05529>
- Meinshausen, M., Nicholls, Z. R. J., Lewis, J., Gidden, M. J., Vogel, E., Freund, M., ... Wang, R. H. J. (2020). The shared socio-economic pathway (ssp) greenhouse gas concentrations and their extensions to 2500. *Geoscientific Model Development*, 13, 3571-3605. Retrieved from <https://gmd.copernicus.org/articles/13/3571/2020/> doi: 10.5194/gmd-13-3571-2020
- Menviel, L., Spence, P., & England, M. H. (2015). Contribution of enhanced antarctic bottom water formation to antarctic warm events and millennial-scale atmospheric co<sub>2</sub> increase. *Earth and Planetary Science Letters*, 413, 37-50. Retrieved from <https://www.sciencedirect.com/science/article/pii/S0012821X14008115> doi: <https://doi.org/10.1016/j.epsl.2014.12.050>
- Müller, J. D., Gruber, N., Carter, B., Feely, R., Ishii, M., Lange, N., ... Zhu, D. (2023). Decadal trends in the oceanic storage of anthropogenic carbon from 1994 to 2014. *AGU Advances*, 4, e2023AV000875. Retrieved from <https://agupubs.onlinelibrary.wiley.com/doi/abs/10.1029/2023AV000875> (e2023AV000875 2023AV000875) doi: <https://doi.org/10.1029/2023AV000875>
- Nissen, C., Timmermann, R., Hoppema, M., Gürses, Ö., & Hauck, J. (2022). Abruptly attenuated carbon sequestration with Weddell Sea dense waters by 2100. *Nature Communications*, 13(1), 3402. doi: 10.1038/s41467-022-30671-3
- Nowicki, S. M. J., Payne, A., Larour, E., Seroussi, H., Goelzer, H., Lipscomb, W., ... Shepherd, A. (2016, 12). Ice sheet model intercomparison project (ismip6) contribution to cmip6. *Geoscientific Model Development*, 9, 4521-4545. Retrieved from <https://www.geosci-model-dev.net/9/4521/2016/> doi: 10.5194/gmd-9-4521-2016
- Noël, B., van Kampenhout, L., van de Berg, W. J., Lenaerts, J. T. M., Wouters, B., & van den Broeke, M. R. (2020). Brief communication: Cesm2 climate forcing (1950–2014) yields realistic greenland ice sheet surface mass balance. *The Cryosphere*, 14, 1425-1435. Retrieved from <https://tc.copernicus.org/articles/14/1425/2020/> doi: 10.5194/tc-14-1425-2020
- Park, W., & Latif, M. (2019, 3). Ensemble global warming simulations with idealized antarctic meltwater input. *Climate Dynamics*, 52, 3223-3239. doi: 10.1007/s00382-018-4319-8
- Pauling, A. G., Bitz, C. M., Smith, I. J., & Langhorne, P. J. (2016). The response of the southern ocean and antarctic sea ice to freshwater from ice shelves in an earth system model. *Journal of Climate*, 29, 1655-1672. doi: 10.1175/JCLI-D-15-0501.1
- Purich, A., & England, M. H. (2023, 1). Projected impacts of antarctic meltwater anomalies over the twenty-first century. *Journal of Climate*, 36, 2703-2719. doi: 10.1175/jcli-d-22-0457.1
- Rignot, E., Mouginot, J., Scheuchl, B., van den Broeke, M., van Wessem, M. J., & Morlighem, M. (2019). Four decades of antarctic ice sheet mass balance from 1979–2017. *Proceedings of the National Academy of Sciences*, 116, 1095-1103. doi: 10.1073/pnas.1812883116
- Rignot, E., Thomas, R. H., Mansley, J. A. D., Corr, H. F. J., Bentley, M. J., Bettadpur, S., ... Zwally, H. J. (2012). Mass balance of polar ice sheets. *Science*, 297, 1502-1506. Retrieved from <http://science.sciencemag.org/content/297/6111/1183> doi: 10.1126/science.1073888
- Sabine, C. L., Feely, R. A., Gruber, N., Key, R. M., Lee, K., Bullister, J. L., ... Rios, A. F. (2004, 7). The oceanic sink for anthropogenic co<sub>2</sub>. *Science*, 305, 367-371. Retrieved from <https://doi.org/10.1126/science.1097403> (doi:



- 10.1126/science.1097403) doi: 10.1126/science.1097403
- Sadai, S., Condron, A., DeConto, R., & Pollard, D. (2020, 9). Future climate response to antarctic ice sheet melt caused by anthropogenic warming. *Science Advances*, 6, eaaz1169. Retrieved from <http://advances.sciencemag.org/> doi: 10.1126/sciadv.aaz1169
- Sarmiento, J. L., Orr, J. C., & Siegenthaler, U. (1992). A perturbation simulation of co<sub>2</sub> uptake in an ocean general circulation model. *Journal of Geophysical Research: Oceans*, 97, 3621-3645. Retrieved from <https://agupubs.onlinelibrary.wiley.com/doi/abs/10.1029/91JC02849> doi: <https://doi.org/10.1029/91JC02849>
- Seroussi, H., Nowicki, S., Payne, A. J., Goelzer, H., Lipscomb, W. H., Abe-Ouchi, A., ... Zwinger, T. (2020). Ismip6 antarctica: a multi-model ensemble of the antarctic ice sheet evolution over the 21st century. *The Cryosphere*, 14, 3033-3070. Retrieved from <https://tc.copernicus.org/articles/14/3033/2020/> doi: 10.5194/tc-14-3033-2020
- Swart, N., Martin, T., Beadling, R., Chen, J.-J., England, M. H., Farneti, R., ... Thomas, M. (2023). The southern ocean freshwater release model experiments initiative (sofia): Scientific objectives and experimental design. *EGUsphere*, 2023, 1-30. Retrieved from <https://egusphere.copernicus.org/preprints/2023/egusphere-2023-198/> doi: 10.5194/egusphere-2023-198
- Swart, N. C., & Fyfe, J. C. (2013, 8). The influence of recent antarctic ice sheet retreat on simulated sea ice area trends. *Geophysical Research Letters*, 40, 4328-4332. doi: 10.1002/GRL.50820
- Swingedouw, D., Bopp, L., Matras, A., & Braconnot, P. (2007). Effect of land-ice melting and associated changes in the amoc result in little overall impact on oceanic co<sub>2</sub> uptake. *Geophysical Research Letters*, 34. Retrieved from <https://agupubs.onlinelibrary.wiley.com/doi/abs/10.1029/2007GL031990> doi: <https://doi.org/10.1029/2007GL031990>
- Terhaar, J., Frölicher, T. L., & Joos, F. (2021). Southern ocean anthropogenic carbon sink constrained by sea surface salinity. *Science Advances*, 7, eabd5964. Retrieved from <https://www.science.org/doi/abs/10.1126/sciadv.abd5964> doi: 10.1126/sciadv.abd5964
- Velicogna, I., Mohajerani, Y., A, G., Landerer, F., Mouginot, J., Noel, B., ... Wiese, D. (2020). Continuity of ice sheet mass loss in greenland and antarctica from the grace and grace follow-on missions. *Geophysical Research Letters*, 47, e2020GL087291. Retrieved from <https://agupubs.onlinelibrary.wiley.com/doi/abs/10.1029/2020GL087291> (e2020GL087291 10.1029/2020GL087291) doi: <https://doi.org/10.1029/2020GL087291>
- von Schuckmann, K., Minière, A., Gues, F., Cuesta-Valero, F. J., Kirchengast, G., Adusumilli, S., ... Zemp, M. (2023). Heat stored in the earth system 1960–2020: where does the energy go? *Earth System Science Data*, 15, 1675-1709. Retrieved from <https://essd.copernicus.org/articles/15/1675/2023/> doi: 10.5194/essd-15-1675-2023
- Wanninkhof, R., Park, G.-H., Takahashi, T., Sweeney, C., Feely, R., Nojiri, Y., ... Khatiwala, S. (2013). Global ocean carbon uptake: magnitude, variability and trends. *Biogeosciences*, 10, 1983-2000. Retrieved from <https://bg.copernicus.org/articles/10/1983/2013/> doi: 10.5194/bg-10-1983-2013